Kinematics Modeling and Analyses of Articulated Rovers

Mahmoud Tarokh and Gregory J. McDermott

***Abstract*—This paper describes a general approach to the kinematics modeling and analyses of articulated rovers traversing uneven terrain. The model is derived for full 6-degree-of-freedom motion, enabling movements in the x,y, and z directions, as well as pitch, roll, and yaw rotations. Differential kinematics is derived for the individual wheel motions in contact with the terrain. The resulting equations of the individual wheel motions are then combined to form the composite equation for the rover motion. Three types of kinematics, i.e., navigation, actuation, and slip kinematics are identified, and the equations and application of each are discussed. The derivations are specialized to Rocky 7, a highly articulated prototype Mars rover, to illustrate the developed methods. Simulation results are provided for the motion of the Rocky 7 over several terrains, and various motion profiles are provided to explain the behavior of the rover.**

***Index Terms*—All-terrain rovers (ATRs), rover kinematics, rover–terrain interaction, slip detection.**

I. Introduction

ARTICULATED all-terrain rovers (ATRs) are a class of mobile robots that have sophisticated mobility systems for enabling their traversal over uneven terrain. These robots are being used increasingly in such diverse applications as planetary explorations [1], rescue operations, mine detection and demining [2], agriculture [3], military missions, inspection, and cleanup operations of hazardous waste storage sites, remote ordinance neutralization, search and recovery, security, and fire fighting.[1] NASA has been very active in the development of ATRs. For example, Rocky series rovers developed at NASA's Jet Propulsion Laboratory (JPL) include Rocky 4, Sojourner (based on the Rocky 4 design and deployed on Mars in July 1997), Rocky 7, and Rocky 8 [1]. More recently, JPL has developed reconfigurable ATRs that have a versatile mobility system, consisting of adjustable arms and shoulders with the goal of adapting and reconfiguring the rover to changes in the terrain topology [4].

Research in the area of mobile robots has seen a tremendous growth in the past ten years. This research can be roughly divided into two areas—one related to high-level tasks, such as path planning, and the other concerning lower level tasks, such as navigation and motion control, which require kinematics modeling and analysis of the robot. Most research efforts on kinematics have concentrated on simple car-like four-wheel mobile robots moving on flat terrain, which we will refer to as ordinary mobile robots (OMRs). The kinematics modeling of these robots can be classified into two main approaches, geometric and transformation. The geometric approach [5], [6] is intuitive, but restrictive if used on its own. The transformation approach is widely employed by researchers, and consists of a series of transformations and their derivatives to relate the motion of the wheels to the motion of the robot. One of the fundamental contributions using this approach is by Muir and Newman [7]. In this paper, a matrix coordinate transformation algebra is developed to derive the equations of the motion of OMRs. Due to the underlying assumptions, this and similar approaches are only applicable to motion in two-dimensional (2-D) space, i.e., translation in the x–y plane and yaw rotation. They also assume perfect rolling motion on a flat, smooth surface with no side or rolling slip, and no motion along the z axis, and thus, the results are not applicable to ATRs.

A number of other researchers have dealt with different aspects of OMR kinematics [8]–[10]. For example, Campion *et al.* [9] present a technique to classify OMRs for the study of the kinematics and dynamics models, while taking into consideration the mobility restriction due to various constraints. The paper by Borestein [10] discusses kinematics of several connected OMRs with compliant linkage. Rajagopalan [11] uses a transformation approach to develop the kinematic model of OMRs with an inclined steering column and different combinations of driving and steering wheels. The forward kinematics of a specific OMR with omnidirectional wheels is derived in [12], and the singularity configurations are identified. Williams *et al.* [13] develop a dynamic model for omnidirectional robots that incorporates a wheel-slip model. Tarokh *et al.* [14] study the kinematics of a particular high-mobility rover. Iagnemma and Dubowsky [15] propose a Kalman-filter approach to estimate the rover wheel-ground contact angle for traction control. Balaram [16] employs a simple kinematics model and a state observer to estimate position, orientation, velocities, and contact angles of a rover.

Despite these efforts, a comprehensive kinematics model of an ATR that can address some of the challenges and problems associated with these rovers has not been developed [17]. The goal of this paper is to propose a methodology for developing a reasonably complete kinematics model of a general ATR and its interaction with the terrain, and to apply this methodology to a particular ATR, i.e., the Rocky 7 Mars rover that has a complex mobility system. Such a model can provide information about

Manuscript received June 1, 2004; revised January 11, 2005. This paper was recommended for publication by Associate Editor K. Yoshida and Editor F. Park upon evaluation of the reviewers' comments. This work was supported in part by a grant from the NASA Jet Propulsion Laboratory (JPL).

The authors are with the Department of Computer Science, San Diego State University, San Diego, CA 92182-7720 USA (e-mail: tarokh@sdsu.edu; greg.mcdermott@baesystems.com).

Digital Object Identifier 10.1109/TRO.2005.847602

[1][Online]. Available: www.jointrobotics.com/activities_new/masterplan.shtml

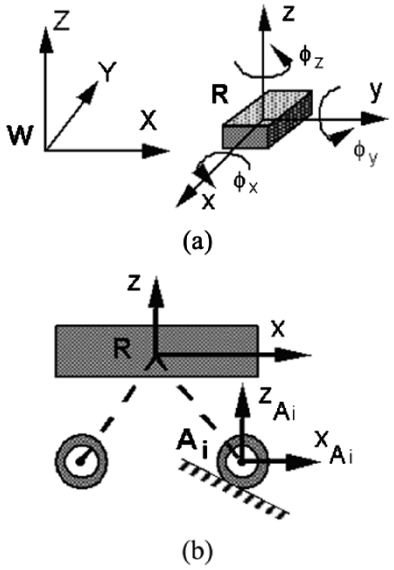

Fig. 1. Geometric description of a generalized ATR. (a) Perspective view. (b) Side view.

various slips, i.e., side, rolling, and turn slips, as described in this paper. This information may be useful for actuation and control to reduce undesirable motions such as sliding, skidding, grinding, and fishtailing. A complete kinematics model is also useful for motion control and navigation of the rover.

In Section II, we describe an approach to developing the kinematics model of a general ATR. Different forms of rover kinematics are discussed in Section III. The rover–terrain interaction is explained in Section IV. Simulation results for the Rocky 7 rover traversing several terrain topologies are presented in Section V. Finally, Section VI provides the conclusions of the paper.

II. Kinematic Model Development

In this section, we develop a general approach to kinematics modeling of an ATR. The emphasis here is on deriving the equations of motion of the rover components relative to a rover reference frame. The rover motion, with respect to a world coordinate system, will be discussed in Section IV, where the interaction of the rover with the terrain will be addressed.

We define an ATR as a wheeled mobile robot consisting of a main body connected to wheels via a set of linkages and joints. The rover is capable of locomotion over uneven terrain by rolling of the wheels and adjusting its joints, and the only contact with the terrain is at the wheel surfaces.

Fig. 1 illustrates the geometric definition of a general ATR. At any time t, the rover has an *instantaneous coordinate frame* R attached to its body that moves with the rover, and is defined relative to a fixed world-coordinate frame. The rover configuration vector $U = [X\ Y\ Z\ \Phi_x\ \Phi_y\ \Phi_z]^T$ is defined relative to the world-coordinate frame W, where (X, Y, Z) is the position, and (Φ_x, Φ_y, Φ_z) is the orientation, with heading Φ_x, pitch Φ_y, and roll Φ_z. The lower-case quantities, i.e., the heading ϕ_x, pitch ϕ_y, and roll ϕ_z in Fig. 1, are with respect to the instantaneous

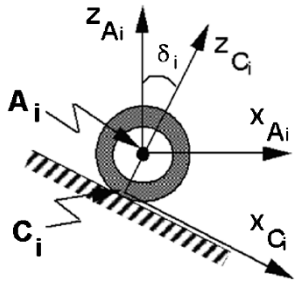

Fig. 2. Coordinate frames for terrain contact at wheel i.

rover frame R. Each rover wheel also has an instantaneous coordinate frame $A_i, i = 1, 2, \ldots, n$ attached to the wheel axle and defined relative to the rover body-coordinate frame R, where n is the number of the wheels. The transformation between the rover-coordinate frame R and each wheel-axle coordinate frame A_i, denoted by the homogeneous transformation $T_{R,Ai}(q)$, depends on the specific rover linkages and joints represented here by the $\nu_q \times 1$ joint variable vector q. The dashed line in Fig. 1(b) represents any set of links and joints that exists between these two frames, including the steering mechanism.

In our analysis, each wheel is assumed to be represented by a rigid disc with a single point of contact with the terrain surface. Allowing multiple contact angles for each wheel makes the kinematics analysis extremely complex. A coordinate frame $C_i, i = 1, \ldots, n$ is defined at each wheel's contact point, as illustrated in Fig. 2, where its x axis is tangent to the terrain at the point of contact, and its z axis is normal to the terrain. The contact angle δ_i is the angle between the z axes of the ith wheel axle and contact coordinate frames, as shown in Fig. 2. This contact angle is a key distinction between an OMR moving on flat surfaces and an ATR traversing uneven terrain. In the former case, the z axis of the contact frame is aligned with the z axis of the wheel axle, and the contact angle is always zero, whereas in the latter case, δ_i is variable. The contact angles play an important role in the kinematics of ATRs.

The contact coordinate frame C_i is obtained from the axle-coordinate frame A_i by rotating δ_i about the axle, then translating by the wheel radius r in the negative z direction. The corresponding transformation matrix from the axle A_i to contact C_i, denoted by $T_{Ai,Ci}$, is given by

$$T_{Ai,Ci}(\delta_i) = \begin{bmatrix} c\delta_i & 0 & s\delta_i & -rs\delta_i \\ 0 & 1 & 0 & 0 \\ -s\delta_i & 0 & c\delta_i & -rc\delta_i \\ 0 & 0 & 0 & 1 \end{bmatrix} \tag{1}$$

where $i = 1, 2, \ldots, n$, and s and c denote sine and cosine.

The transformation from the rover-reference frame to wheel-contact frame C_i is thus $T_{R,Ci}(q, \delta_i) = T_{R,Ai}(q) T_{Ai,Ci}(\delta_i)$. However, this transformation does not include rolling or slip, and thus does not reflect motion. In order to include motion, we consider the instantaneous contact frames $C_i(t - \Delta t)$ and $C(t)$, where Δt is a time increment, as shown in Fig. 3.

The wheel motion from $C_i(t - \Delta t) \equiv \bar{C}_i$ to $C_i(t) \equiv C_i$ is defined by a coordinate transformation corresponding to a wheel-rolling translation $(r\theta_i + \xi_i)$ along the x axis, where θ_i is the angular rotation, and ξ_i is the rolling slip, a wheel side-slip

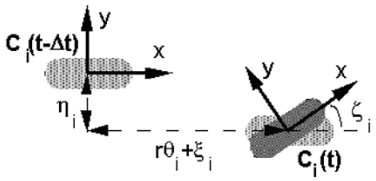

Fig. 3. Incremental motion by rolling and slip.

translation η_i along the y axis, and a turn-slip rotation ζ_i about the z axis. Thus

$$T_{\bar{C}_i,C_i} = \begin{bmatrix} c\zeta_i & s\zeta_i & 0 & r\theta_i + \xi_i \\ s\zeta_i & c\zeta_i & 0 & \eta_i \\ 0 & 0 & 1 & 0 \\ 0 & 0 & 0 & 1 \end{bmatrix}. \tag{2}$$

Note that the z component of the translation motion is zero, since no movement along the z axis is allowed, due to the fact that jumping of the wheel off the terrain or penetration of the wheel into the terrain is assumed not to occur.

The transformation from a wheel-contact frame at time $t-\Delta t$ denoted by $\bar{C}_i$ to the rover frame R is

$$T_{\bar{C}i,R} = T_{\bar{C}i,Ci}(\theta_i, \varepsilon_i) T_{Ci,Ai}(\delta_i) T_{Ai,R}(q) \tag{3}$$

where $\varepsilon_i = [\xi_i \;\; \zeta_i \;\; \eta_i]^T$ is the slip vector, $T_{Ci,Ai}(\delta_i) = (T_{Ai,Ci}(\delta_i))^{-1}, T_{Ai,R}(q) = (T_{R,Ai}(q))^{-1}$, and the dependencies of the transformation matrices are shown with quantities inside the brackets.

To quantify the motion, we must relate changes in the rover configuration-rate vector $\dot{u} = [\dot{x} \;\; \dot{y} \;\; \dot{z} \;\; \dot{\phi}_x \;\; \dot{\phi}_y \;\; \dot{\phi}_z]^T$ to the rover joint-angle rates $\dot{q}$, wheel-roll rates $\dot{\theta}_i$, and wheel slip-rate vector $\dot{\varepsilon}_i$. To do this, we consider the matrix $T_{\bar{R},R}$ that describes the transformation from the rover frame at time $t - \Delta t$ to the rover frame at time t, which can be written as $T_{\bar{R},R} = T_{\bar{R},\bar{C}i} T_{\bar{C}i,R}$. Since $T_{\bar{R},\bar{C}i}$ is independent of time, the derivative of $T_{\bar{R},R}$ is

$$\dot{T}_{\bar{R},R} = T_{\bar{R},\bar{C}i} \dot{T}_{\bar{C}i,R}. \tag{4}$$

The transformation derivative $\dot{T}_{\bar{C}i,R}$ defines the motion of the rover reference frame R relative to the wheel i coordinate frame $\bar{C}_i$. For a specific rover, $T_{\bar{C}i,R}$ exists as given by (3), and its derivative can be computed as

$$\dot{T}_{\bar{C}i,R} = \frac{\partial T_{\bar{C}i,R}}{\partial q}\dot{q} + \frac{\partial T_{\bar{C}i,R}}{\partial \theta_i}\dot{\theta}_i + \frac{\partial T_{\bar{C}i,R}}{\partial \varepsilon_i}\dot{\varepsilon}_i + \frac{\partial T_{\bar{C}i,R}}{\partial \delta_i}\dot{\delta}_i. \tag{5}$$

We evaluate the partial derivatives in (5) at the reference condition. Now, $\dot{T}_{\bar{R},R}$ can also be found for a general body in motion, using the position and orientation rates as [18]

$$\dot{T}_{\bar{R},R} = \begin{bmatrix} 0 & -\dot{\phi}_z & \dot{\phi}_y & \dot{x} \\ \dot{\phi}_z & 0 & -\dot{\phi}_x & \dot{y} \\ -\dot{\phi}_y & \dot{\phi}_x & 0 & \dot{z} \\ 0 & 0 & 0 & 1 \end{bmatrix}. \tag{6}$$

Note that $\dot{T}_{\bar{R},R}$ is a skew-symmetric matrix, and the transformation-product matrix on the right-hand side of (4) also has the structure of (6). Substituting (5) and (6) into (4), evaluating the matrix product, and equating the like matrix elements on both sides of the resulting equation, we can determine rover configuration-rate vector $\dot{u}$ in terms of the joint angular-rates vector $\dot{q}$, contact-angle rate $\dot{\delta}_i$, wheel-rolling rate $\dot{\theta}_i$, and wheel slip-rate vector $\dot{\varepsilon}_i$. Furthermore, these equations are linear in the time derivatives $\dot{q}, \dot{\theta}_i, \dot{\delta}_i, \dot{\varepsilon}_i$, as seen from (5). These lead to an equation of the form

$$[\dot{x} \;\; \dot{y} \;\; \dot{z} \;\; \dot{\phi}_x \;\; \dot{\phi}_y \;\; \dot{\phi}_z]^T = J_i [\dot{q} \;\; \dot{\theta}_i \;\; \dot{\varepsilon}_i \;\; \dot{\delta}_i]^T \tag{7}$$

where J_i is the $6 \times (\nu_q + 5)$ wheel Jacobian matrix, and ν_q is the dimension of the joint vector q. Equation (7) describes the contribution of individual wheel motion and the connecting joints to the rover body motion. The net body motion is the composite effect of all wheels, and can be obtained by combining (7) into a single matrix equation as

$$\begin{bmatrix} I_6 \\ I_6 \\ \vdots \\ I_6 \end{bmatrix} \begin{bmatrix} \dot{x} \\ \dot{y} \\ \dot{z} \\ \dot{\phi}_x \\ \dot{\phi}_y \\ \dot{\phi}_z \end{bmatrix} = J \begin{bmatrix} \dot{q} \\ \dot{\theta} \\ \dot{\varepsilon} \\ \dot{\delta} \end{bmatrix} \quad \text{or} \quad E\dot{u} = J\dot{p} \tag{8}$$

where E is a $6n \times 6$ matrix that is obtained by stacking n 6×6 identity matrices, $\dot{q}$ is the $\nu_q \times 1$ vector of rover joint angles, $\dot{\theta}$ is the $n \times 1$ vector of wheel-rolling rates, $\dot{\varepsilon}$ is the $3n \times 1$ vector consisting of rolling $\dot{\xi}$, turn $\dot{\zeta}$, and side $\dot{\eta}$ slip rates, and $\dot{\delta}$ is the $n \times 1$ vector of contact-angle rates. The rover Jacobian matrix J is a $6n \times (\nu_q + 5n)$ matrix formed from the individual wheel Jacobian matrices $J_i, i = 1, 2, \ldots, n$, and $\dot{p}$ is the $(\nu_q + 5n) \times 1$ vector of composite angular rates. Observe from (7) and (8) that J is a sparse matrix. In the following section, we apply the above kinematics modeling to an articulated planetary rover.

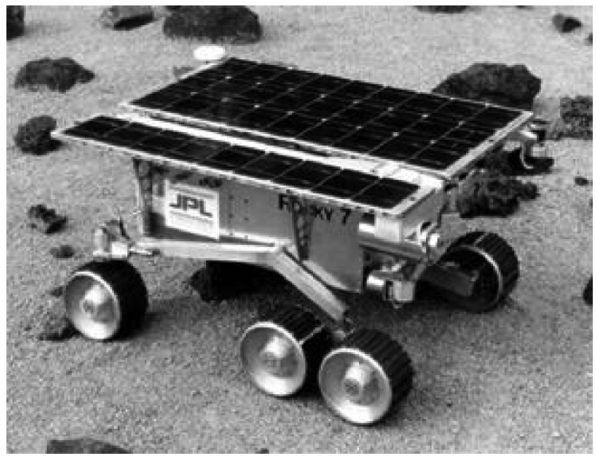

Fig. 4. Rocky 7 Mars rover.

A. Example: Rocky 7 Mars Rover

The Rocky 7 prototype Mars rover was designed by NASA's JPL for missions requiring long traverses over rough terrain. It has a relatively complex mobility system, enabling it to climb over rocks. A description of Rocky 7 rover including science instruments is given in [1]. In this section, we describe only those attributes relevant to the kinematic modeling of the rover.

Rocky 7 consists of six wheels using a rocker-bogie design, as illustrated in Fig. 4. The rover is approximately 48 cm wide, 64 cm long, and 32 cm high, and each wheel has a diameter of 13 cm. A main rocker is hinged to each side of the body. Figs. 4 and 5 show the left side of the rover and the left main rocker. Each

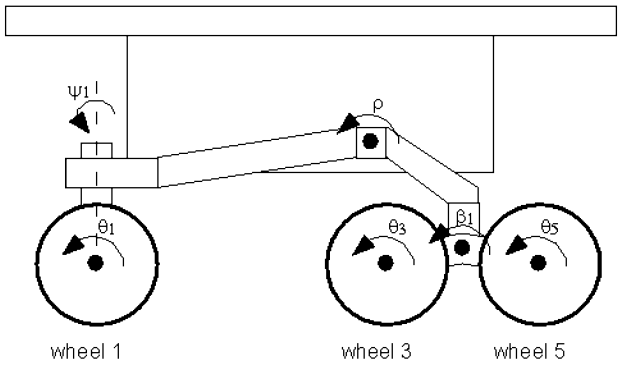

Fig. 5. Schematic diagram of Rocky 7 rover showing joint angles and wheel-rolling angles.

main rocker has a steerable front wheel at one end (wheel 1 in Fig. 5), and a smaller rocker at the other end. Two nonsteerable back wheels (3 and 5 in Fig. 5) are attached to the smaller rockers. The right side similarly consists of the front wheel 2 and back wheels 4 and 6. The main rocker is connected to the smaller rocker via a joint called the bogie joint, with an angle denoted by β_1 for the left side (Fig. 5) and β_2 for the right side. When the rover moves over a flat surface $\beta_1 = \beta_2 = 0$ and when the back wheels climb rocks, these angles become nonzero.

The two main rockers are connected to the body via a differential such that the left and right rocker angles, denoted by ρ_1 and ρ_2, respectively, can be represented by a single joint angle $\rho = \rho_1 = -\rho_2$ (Fig. 5). On a flat surface, the rocker angle is zero, but becomes nonzero when one side moves up or down with respect to the other side. The rocker-bogie joints ρ, β_1, and β_2 are unactuated and provide for compliance with the terrain. These joint angles are measured by potentiometers. The two steerable front wheels are measured by encoders, and have steering angles ψ_1 and ψ_2 with a physical steering range of 270°. Thus, Rocky 7 joint-angle vector q consists of rocker-bogie and steering angles, i.e., $q = [\rho\ \beta_1\ \beta_2\ \psi_1\ \psi_2]^T$.

Each wheel is actuated independently, and its angular rotation θ_i is measured by an encoder. The Rocky 7 rover senses body pitch and body roll via accelerometers. A sun sensor is available to compute heading information based on the rover's location, pitch, roll, and time of day. Furthermore, an inertial-rate gyro is available to measure motion, but must periodically be adjusted to correct for drift.

Fig. 6(a) illustrates our choice of coordinate frames for the left side of Rocky 7, which includes wheels 1 (left front wheel), and 3 and 5 (left back wheels). The right side (not shown) is assigned similar frames and consists of wheels 2, 4, and 6. In Fig. 6, R is the rover reference frame, D is the differential frame, B1 and B2 are left and right bogie joint frames, and Si, Ai, and Ci are the steering, axle, and contact frames, respectively, for wheel $i = 1, 2, \ldots, 6$. Fig. 6(b) shows the detailed side view of the two left back wheels and the left bogie coordinate frame.

The Denavit–Hartenberg (D–H) parameters γ, d, a, and α for Rocky 7 are given in Table I with units degrees, centimeters, centimeters, and degrees, respectively. The constants k_i in Fig. 6 represent distances and angles as defined in Table I.

The coordinate frames in Fig. 6 were selected for consistency with D–H notation. For example, the differential frame D is obtained from the rover reference R by translating $d = k_1$ along the z axis, translating $a = k_2$ along the x axis, and rotating $\alpha = -90°$ about the x axis. Similarly, the steering frames Si and axle frames Ai are obtained using Table I. Each coordinate frame represents one step in the kinematics chain from the rover's reference frame R to a wheel contact Ci $(i = 1, 2, \ldots, 6)$, which can be written as

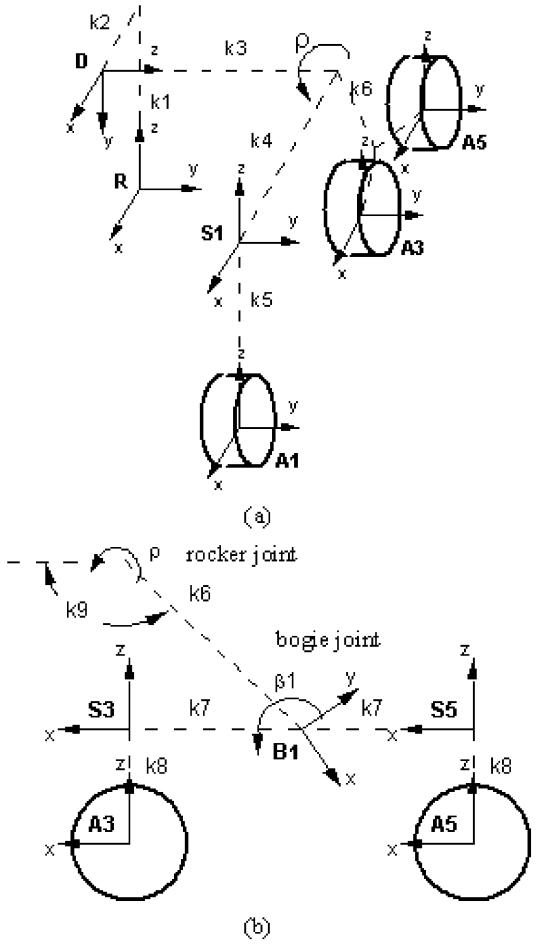

Fig. 6. Coordinate frames for rover's left side. (a) Reference R, differential D, steering S1, and axle Ai $(i = 1, 3, 5)$ coordinate frames. (b) Bogie B1, steering Si, and axle Ai $(i = 3, 5)$ frames.

$$
\begin{aligned}
T_{R,Ci} &= (T_{R,D})(T_{D,Si})(T_{Si,Ai})(T_{Ai,Ci}), \quad i = 1, 2 \\
T_{R,Ci} &= (T_{R,D})(T_{D,B1})(T_{B1,Si})(T_{Si,Ai})(T_{Ai,Ci}), \quad i = 3, 5 \\
T_{R,Ci} &= (T_{R,D})(T_{D,B2})(T_{B2,Si})(T_{Si,Ai})(T_{Ai,Ci}), \quad i = 4, 6.
\end{aligned} \tag{9}
$$

The transformations from axle frames to contact frames, $T_{Ai,Ci}$, are given by (1) rather than by D–H parameters, and therefore, no entries for the contact frames are provided in Table I. The other transformation matrices in (9) are obtained from Table I. Substituting these transformation matrices in (9) and simplifying, the rover reference frame to the contact transformation matrices for wheels 1 and 2 of Rocky 7 are found to be

$$
T_{R,Ci} = \begin{bmatrix}
(c\psi_i c\rho c\delta_i + b_i s\rho s\delta_i & -s\psi_i c\rho & T_{1,3} & T_{1,4} \\
s\psi_i c\delta_i & c\psi_i & s\psi_i s\delta_i & T_{2,4} \\
(b_i c\psi_i c\rho c\delta_i - c\rho s\delta_i & -b_i s\psi_i s\rho & T_{3,3} & T_{3,4} \\
0 & 0 & 0 & 1
\end{bmatrix}, \quad i = 1, 2 \tag{10}
$$

TABLE I
D–H PARAMETERS FOR ROCKY 7

Frame	γ	d	a	α
D	0	k_1	k_2	-90
B1	$k_9 + \rho$	k_3	k_6	0
B2	$k_9 - \rho$	$-k_3$	k_6	0
S1	ρ	k_3	k_4	90
S2	$-\rho$	$-k_3$	k_4	90
S3	$\beta_1 - k_9$	0	k_7	90
S4	$\beta_2 - k_9$	0	k_7	90
S5	$\beta_1 - k_9$	0	$-k_7$	90
S6	$\beta_2 - k_9$	0	$-k_7$	90
A1	ψ_1	$-k_5$	0	0
A2	ψ_2	$-k_5$	0	0
A3	0	$-k_8$	0	0
A4	0	$-k_8$	0	0
A5	0	$-k_8$	0	0
A6	0	$-k_8$	0	0

k_1 = 10.5 cm - vertical offset between rover reference (R) to differential (D)
k_2 = 12.075 cm - forward offset between R and D
k_3 = 20.0 cm - horizontal distance between D and wheels
k_4 = 28.8 cm - distance from D to steering axis of front wheels
k_5 = 12.5 cm - height of D from wheel axles
k_6 = 16.0 cm - length of link from rocker joint to bogie joint
k_7 = 6.9 cm - length from bogie joint to forward/rear bogie
k_8 = 2.0 cm - height of bogie joint from wheel axles
k_9 = 139.0 deg - angle of link between rocker and bogie joints
k_{10} = 6.5 cm - wheel radius

where $b_i = (-1)^i$ and

$$\begin{aligned}
T_{1,3} &= c\psi_i c\rho s\delta_i - b_i s\rho c\delta_i \\
T_{3,3} &= b_i c\psi_i s\rho s\delta_i + c\rho c\delta_i \\
T_{1,4} &= b_i k_5 s\rho + k_4 c\rho - k_1 T_{1,3} \\
T_{2,4} &= -b_i k_3 - k_1 s\psi_i s\delta_i \\
T_{3,4} &= -k_5 c\rho + b_i k_4 s\rho - k_1 T_{3,3}.
\end{aligned}$$

The position and orientation of the wheel at the contact points for the front wheels can be extracted from the transformation matrix (10), e.g., $x_i = T_{14}, y_i = T_{24}, z_i = T_{34}$. Note that in the special case where the rover moves over a flat surface $\delta_i = \rho = 0$, then (10) reduces to a rotation of ψ_i about the$z$ axis, and translations k_4 along the x axis, k_3 along the y axis for wheel 1 ($-k_3$ for wheel 2), and $-k_5$ along the z axis.

Similarly, the transformation matrices for the back wheels 3–6 are found using (1), (9), and Table I as

$$T_{R,Ci} = \begin{bmatrix} c\sigma_i & 0 & s\sigma_i & T_{1,4} \\ 0 & 1 & 0 & -b_i k_3 \\ -s\sigma_i & 0 & c\sigma_i & T_{3,4} \\ 0 & 0 & 0 & 1 \end{bmatrix}, \quad i = 3,4,5,6 \quad (11)$$

where now

$$\begin{aligned}
T_{1,4} &= k_6 c(k_9 - b_i\rho) + a_{Si} c(\sigma_i - \delta_i) - k_5 s(\sigma_i - \delta_i) - k_1 s\sigma_i \\
T_{3,4} &= -k_6 s(k_9 - b_i\rho) - a_{Si} s(\sigma_i - \delta_i) - k_5 c(\sigma_i - \delta_i) - k_1 c\sigma_i \\
\sigma_i &= \begin{cases} \rho + \beta_1 + \delta_i, & i = 3,5 \\ -\rho + \beta_2 + \delta_i, & i = 4,6 \end{cases} \\
a_{Si} &= \begin{cases} k_7, & i = 3,4 \\ -k_7, & i = 5,6. \end{cases}
\end{aligned}$$

It is noted that the rover-contact transformations $T_{R,Ci}$ are functions of rover joint angles $\rho, \beta_1, \beta_2, \psi_1, \psi_2$, and contact angle δ_i.

The rover Jacobian equations are derived from (2)–(7) using (10) and (11). This involves first forming $T_{\bar{C}i,R} = T_{\bar{C}i,C} T_{C,R}$ via (2), (10), and (11), and taking its derivative with respect to the joint-angle vector $q = [\rho\ \beta_1\ \beta_2\ \psi_1\ \psi_2]$, contact angle δ_i, wheel rotation θ_i, and slip vector $\varepsilon_i = [\zeta_i\ \xi_i\ \eta_i]^T$ to obtain $\dot{T}_{\bar{C}i,R}$, as in (5). The acquired $\dot{T}_{\bar{C}i,R}$, and $\dot{T}_{\bar{R},R}$ given by (6) are substituted in (4), and the like elements of the matrices in both sides of (4) are equated. This gives an equation of the form (7) relating the rover position/orientation rates to the rover joint-angle rates. The resulting equation for wheels 1 and 2 is

$$\begin{bmatrix} \dot{x} \\ \dot{y} \\ \dot{z} \\ \dot{\phi}_x \\ \dot{\phi}_y \\ \dot{\phi}_z \end{bmatrix} = \begin{bmatrix} -b_i k_1 & J_{x,\psi} & J_{x,\theta} & J_{x,\xi} & J_{x,\zeta} & J_{x,\eta} & J_{x,\delta} \\ 0 & J_{y,\psi} & J_{y,\theta} & J_{y,\xi} & J_{y,\zeta} & J_{y,\eta} & J_{y,\delta} \\ b_i k_2 & J_{z,\psi} & J_{z,\theta} & J_{z,\xi} & J_{z,\zeta} & J_{z,\eta} & J_{z,\delta} \\ 0 & J_{\phi x,\psi} & 0 & 0 & J_{\phi x,\zeta} & 0 & J_{\phi x,\delta} \\ b_i & 0 & 0 & 0 & J_{\phi y,\zeta} & 0 & J_{\phi y,\delta} \\ 0 & J_{\phi z,\psi} & 0 & 0 & J_{\phi z,\zeta} & 0 & J_{\phi z,\delta} \end{bmatrix} \times \begin{bmatrix} \dot{\rho} \\ \dot{\psi}_i \\ \dot{\theta}_i \\ \dot{\xi}_i \\ \dot{\zeta}_i \\ \dot{\eta}_i \\ \dot{\delta}_i \end{bmatrix}, \quad i = 1,2. \quad (12)$$

The first column of J shows that the rocker angle contributes only to $\dot{x}, \dot{z}$, and pitch $\dot{\phi}_y$. The third, fourth, and sixth columns indicate that the rolling velocity, rolling slip, and side slip have no effect on the orientation of the rover. The contributions of various rover angles to the forward rover velocity $\dot{x}$ are given by the first row of the Jacobian matrix, whose elements are

$$\begin{aligned}
J_{x,\psi} &= b_i k_3 c\rho \\
J_{x,\theta} &= k_{10}(b_i s\rho s\delta_i + c\rho c\psi_i c\delta_i) \\
J_{x,\xi} &= (b_i s\rho s\delta_i + c\rho c\psi_i c\delta_i) \\
J_{x,\zeta} &= -k_5 c\rho s\psi_i s\delta_i - b_i k_4 s\rho s\psi_i s\delta_i - k_3 s\rho c\psi_i s\delta_i \\
&\quad - b_i k_3 c\rho c\delta_i - k_1 s\psi_i \delta_i \\
J_{x,\eta} &= -s\psi_i c\rho \\
J_{x,\delta} &= -k_5 c\rho c\psi_i + b_i k_4 s\rho c\psi_i - k_3 s\rho s\psi_i + k_1 c\psi_i.
\end{aligned}$$

It is seen from $J_{x,\psi}$ that the rocker angle attenuates the effect of steering rate on the forward rover velocity $\dot{x}$ through a simple equation. The other components of rover joint rates modify $\dot{x}$ in a more complex manner involving rocker, steering, and contact angles. Furthermore, the above equations can be used to study the manner in which various angles affect the forward velocity in special cases, e.g., rover moving on a ramp, a hill-like, or a flat surface. The elements of the second to sixth rows of the Jacobian matrix are given in the Appendix.

The Jacobian matrices for wheels 3–6 are obtained similarly to those of wheels 1 and 2, and are shown in (13) at the bottom of the next page. The elements of the above Jacobian matrices are given in the Appendix. Compared with the two front wheels, the Jacobian matrices of the back wheels are more sparse. Furthermore, instead of the steering angles, the bogie angles β_1, β_2 now appear in the equations.

III. Forms of Rover Kinematics

The composite equation (8), reflecting the contribution of various angular rates to the overall motion of the rover, can be cast in several forms, depending on the specific situation of interest. In this paper, we will discuss three useful forms of (8), which we refer to as navigation kinematics, slip kinematics, and actuation kinematics. These kinematics forms can be used within a control scheme to improve navigation, to determine proper actuation of the wheels, such as during path following, and to detect and reduce slip by proper maneuvering. However, in this paper, our emphasis is the development of the rover kinematics, rather than control aspects of the rover.

A. Navigation Kinematics

Navigation kinematics relates rover position/heading rate and other quantities of interest to the sensed quantities, such as wheel-roll rate and joint-angle rates. Navigation kinematics is of little use on its own for dead-reckoning, due to errors and noise. However, it is useful for better understanding of the role of different quantities that contribute to the rover position and orientation.

Joint-angle measurement may be available on some rover joints, and encoders may be installed on some or all wheels for measuring rolling rates. In addition, some rovers are equipped with accelerometers for pitch and roll angle measurements. Thus, we must separate the sensed/known and not-sensed/unknown quantities in (8) as

$$[E_s \quad E_n]\begin{bmatrix}\dot{u}_s\\ \dot{u}_n\end{bmatrix} = [J_s \quad J_n]\begin{bmatrix}\dot{p}_s\\ \dot{p}_n\end{bmatrix} \tag{14}$$

where the 6×1 position/orientation vector $\dot{u}$ is partitioned into the $\mu_n \times 1$ vector of not-sensed quantities $\dot{u}_n$ (e.g., $\dot{x}, \dot{y}, \dot{z}$, and yaw rate $\dot{\phi}_z$) and the $\mu_s \times 1 = (6-\mu_n)\times 1$ vector of sensed quantities $\dot{u}_s$ (e.g., pitch and roll measured by accelerometers). Similarly, the $(\nu_q + 5n)\times 1$ rover angular velocity vector $\dot{p} = [\dot{q}\ \dot{\theta}\ \dot{\varepsilon}\ \dot{\delta}]^T$ is partitioned into a $\nu_n \times 1$ vector of not-sensed quantities, and the $\nu_s \times 1 = (\nu_q + 5n - \nu_n)\times 1$ vector of sensed quantities. Generally, joint angle-rate vector $\dot{q}$ and wheel angular velocities $\dot{\theta}$ are all sensed, whereas contact angle-rate vector $\dot{\delta}$ and the slip-rate vector $\dot{\varepsilon}$ are not sensed. The matrices E_n, E_s, J_n, and J_s in (14) have dimensions $6n\times\mu_n, 6n\times\mu_s, 6n\times\nu_n$, and $6n\times\nu_s$, respectively. Rearranging (14) into sensed (known) and not-sensed (unknown) quantities, we obtain

$$[E_n \quad -J_n]\begin{bmatrix}\dot{u}_n\\ \dot{p}_n\end{bmatrix} = [-E_s \quad J_s]\begin{bmatrix}\dot{u}_s\\ \dot{p}_s\end{bmatrix} \ \text{ or } \ A\chi = B\omega \tag{15}$$

where χ and ω are, respectively, the $(\mu_n+\nu_n)\times 1$ and $(\mu_s+\nu_s)\times 1$ vectors of not-sensed and sensed quantities, respectively, and A and B are matrices of dimensions $6n\times(\mu_n+\nu_n)$ and $6n\times(\mu_s+\nu_s)$, respectively. In navigation kinematics, we are mainly interested in finding the position and the heading of the rover, i.e., $\dot{u}_n$ in (15).

Depending on the rank of A, (15) may or may not have a unique solution. There exists a unique solution if rank $(A|B) =$ rank $(A) = \mu_n + \nu_n$. On the other hand, if rank $(A|B) >$ rank (A), the system is overdetermined, and a unique solution exists, provided that rank $(A|B\omega) =$ rank $(A) = \mu_n + \nu_n$, otherwise the equations are inconsistent. Finally, if rank $(A) < \mu_n+\nu_n$, the equations are underdetermined, and no unique solutions exist. It is clear that when wheel-rolling velocity cannot be measured independently of rolling slip, or when steering rate is indistinguishable from turn slip, the matrix A becomes rank-deficient. The ranks of the above matrices also depend on the kinematics arrangement of sensors used on the particular rover under consideration. This type of analysis may be useful for evaluating alternative rovers and sensor configurations for ample sensing.

We can solve (15) with a least-squares method if rank $(A) = \mu_n + \nu_n$. The solution to (15) is obtained by forming the error vector

$$e = A\chi - B\omega \tag{16}$$

and finding the unknown vector χ that minimizes the weighted error $(e^T We)$, where $W = \text{diag}\{W_1 \ldots W_{\mu n+\nu n}\}$ is a weighting matrix with block diagonal structure, and W_i are the individual wheel-weighting matrices. For simplicity, these weighting matrices are chosen to be of the form $W_i = \lambda_i S$, where S is a constant diagonal scaling matrix, and λ_i is a scalar weight for wheel i. The matrix S is used to scale equations with different units, such as position rates relative to angular rates. The solution to (15), subject to $\min(e^T We)$, is

$$\chi = (A^T W A)^{-1} A^T W B\omega. \tag{17}$$

The navigation quantity $\dot{u}_n$ can be extracted by taking the first μ_n elements of χ. When the system is overdetermined, i.e., rank $(A|B) > (\mu_n + \nu_n)$, we have ample sensing. This is highly desirable, because it provides extra sensing capability, and this information can be exploited for error analysis in situations where the equations are inconsistent. Ample sensing is also useful, in case some sensors fail or provide erroneous data. Furthermore, the equations of motion may be inconsistent due to wheel slip, rover sliding, and bouncing, etc. Ample sensing provides improved navigation estimates under these conditions.

$$\begin{bmatrix}\dot{x}\\ \dot{y}\\ \dot{z}\\ \dot{\phi}_x\\ \dot{\phi}_y\\ \dot{\phi}_z\end{bmatrix} = \begin{bmatrix} -b_i k_1 & J_{x,\beta_1} & J_{x,\beta 2} & k_{10} c\sigma_i & c\sigma_i & J_{x,\zeta} & 0 & J_{x,\delta}\\ 0 & 0 & 0 & 0 & 0 & J_{y,\zeta} & 1 & 0\\ b_i k_2 & J_{z,\beta 1} & J_{z,\beta 2} & -k_{10} s\sigma_i & -s\sigma_i & J_{z,\zeta} & 0 & J_{z,\delta}\\ 0 & 0 & 0 & 0 & 0 & s\sigma_i & 0 & 0\\ b_i & J_{\phi y,\beta 1} & J_{\phi y,\beta 2} & 0 & 0 & 0 & 0 & -1\\ 0 & 0 & 0 & 0 & 0 & c\sigma_i & 0 & 0\end{bmatrix}\begin{bmatrix}\dot{\rho}\\ \dot{\beta}_1\\ \dot{\beta}_2\\ \dot{\theta}_i\\ \dot{\xi}_i\\ \dot{\zeta}_i\\ \dot{\eta}_i\\ \dot{\delta}_i\end{bmatrix}, \quad i = 3,4,5,6 \tag{13}$$

The least-squared residual error is also informative concerning navigation uncertainty. A large least-squares error implies larger navigational uncertainty, while a small error is a reflection of more accurate navigation estimates.

B. Slip Kinematics

Various slips, i.e., turn slip ζ_i, roll slip ξ_i, and side slip η_i provide information about the rover behavior. This information, when processed, can be used for proper actuation and control to reduce undesirable motions, such as sliding and skidding. The magnitude of slip conditions helps determine the magnitude of corrective action, such as braking and steering. However, these control aspects are outside the scope of this paper, and will not be discussed here.

In order to determine the slip vector, we partition the quantities in (7) into the sensed and not-sensed quantities for each individual wheel. As in the case of navigation kinematics, we also partition the rover position/orientation vector $\dot{u}$ and joint-angle vector $\dot{q}$ into sensed and not-sensed components, and rearrange (7) as

$$[I_{\mu n} \quad -J_{in}] \begin{bmatrix} \dot{u}_n \\ \dot{q}_n \\ \dot{\varepsilon}_i \\ \dot{\delta}_i \end{bmatrix} = [-I_{\mu s} \quad J_{is}] \begin{bmatrix} \dot{u}_s \\ \dot{q}_s \\ \dot{\theta}_i \end{bmatrix}, \quad i = 1, 2, \ldots, n \tag{18}$$

where it is assumed that the wheel i contact angle is unknown, but the wheel-rolling velocity is measured, as is usually the case. In the above equation, $I_{\mu n}$ and $I_{\mu s}$ are, respectively, the $6 \times \mu_n$ and $6 \times \mu_s$ submatrices of the 6×6 identity matrix with $(\mu_s + \mu_n) = 6$. Similarly, J_{in} and J_{is} are, respectively, $6 \times (\nu_{qn} + 4)$ and $6 \times (\nu_{qs} + 1)$ submatrices of J_i in (7) where ν_{qn} and ν_{qs} are the dimensions of sensed and not-sensed joint-rate vectors $\dot{q}_n$ and $\dot{q}_s$, respectively. Equation (18) can be put into a more compact form as

$$A_i \chi_i = B_i \omega_i, \quad i = 1, 2, \ldots, n \tag{19}$$

where the quantities in (19) are defined in (18), and the dimensions of A_i and B_i are $6 \times (\mu_n + \nu_{qn} + 4)$ and $6 \times (\mu_s + \nu_{qs} + 1)$, respectively. The analyses of the existence of a solution to (19) are very similar to those of the navigation kinematics case. The wheel i slip rates can be detected if rank $(A_i | B_i \omega_i) =$ rank$(A_i) = \mu_n + \nu_{qn} + 4$, and the solution can be found using a least-squares approach similar to (17).

C. Actuation Kinematics

The actuation kinematics determines the commands to wheel and steering motors based on the desired rover body motion. As in the navigation kinematics, some quantities are sensed and others are not. However, in the case of actuation kinematics, the desired rover motions, such as rover velocity $\dot{x}_d$ and yaw rate $\dot{\phi}_{z_d}$ must also be specified. Furthermore, since it is desirable to actuate wheels and steering to reduce or remove rolling and side slip, we can specify $\varepsilon_d = [\dot{\xi}_d \ \ \dot{\eta}_d]^T = [0 \ \ 0]^T$. This is equivalent to removing these components from the Jacobian equations. The position-orientation rate vector $\dot{u}$ is partitioned as $\dot{u} = [\dot{u}_d \ \ \dot{u}_s \ \ \dot{u}_n]^T$, where $\dot{u}_d$ is the $\mu_d \times 1$ vector of desired quantities, and $\dot{u}_s$ and $\dot{u}_n$ are as defined before. The joint-angle vector q is partitioned as $q = [q_a \ \ q_{us} \ \ q_{un}]^T$, where q_a is the $\nu_a \times 1$ vector of actuated joint angles (e.g., steering angle), q_{us} is the $\nu_{us} \times 1$ vector of unactuated but sensed joint angles, and q_{un} is the $\nu_{un} \times 1$ vector of unactuated and not-sensed joint angles. The $n \times 1$ wheel-rolling angle vector is partitioned similarly into the $\nu_{\theta a} \times 1$ vector of actuated roll angles θ_a, the $\nu_{\theta us} \times 1$ vector of unactuated but sensed angles θ_{us}, and the $\nu_{\theta un} \times 1$ unactuated and not sensed wheel-rolling angles θ_{un}, that is, $\theta = [\theta_a \ \ \theta_{us} \ \ \theta_{un}]^T$. The $3n \times 1$ slip vector ε and the $n \times 1$ contact-angle vector δ are generally unknown. Rearranging (8) into known and unknown quantities, we obtain

$$[E_n \quad -J_{an}] \begin{bmatrix} \dot{u}_n \\ \dot{q}_a \\ \dot{q}_{\text{un}} \\ \dot{\theta}_a \\ \dot{\theta}_{\text{un}} \\ \dot{\zeta} \\ \dot{\delta} \end{bmatrix} = [-E_{ds} \quad J_{as}] \begin{bmatrix} \dot{u}_d \\ \dot{u}_s \\ \dot{q}_s \\ \dot{\theta}_{\text{us}} \end{bmatrix} \tag{20}$$

where E_n and E_{ds} are, respectively, the $6n \times \mu_n$ and $6n \times \mu_{ds}$ matrices formed from the $6n \times 6n$ identity matrices, with $\mu_{ds} + \mu_n = 6$. Matrices J_{an} and J_{as} have dimensions $6n \times \nu_{an}$ and $6n \times \nu_{as}$, respectively, where $\nu_{an} = \nu_{q_a} + \nu_{q_{un}} + \nu_{\theta a} + \nu_{\theta un} + 2n$ and $\nu_{as} = \nu_{qs} + \nu_{\theta us}$. The purpose of the actuation kinematics is to find the actuated joint-angle rate vector $\dot{q}_a$ (e.g., steering) and rolling rate $\dot{\theta}_a$ to accomplish the desired body motion $\dot{u}_d$. The other quantities on the left-hand side (LHS) of (20) are found as a by-product. Note that (20) is of similar form to (15), and can be put into the more compact form

$$A_a \chi_a = B_a \omega_a \tag{21}$$

where χ_a is the $(\mu_n + \nu_{an})$ vector of actuated and unknown quantities, and ω_a is the $(\mu_{ds} + \nu_{as})$ vector of desired and sensed quantities. The matrices A_a and B_a have dimensions $6n \times (\mu_n + \nu_{an})$ and $6n \times (\mu_{ds} + \nu_{as})$, respectively. Since (21) has the same form as (15), the conditions for existence of a unique solution to (21) can be obtained similarly to those explained for (15). In particular, when the matrix A_a is full rank and rank $(A_a | B_a) =$ rank(A_a), a unique solution exists and is obtained from

$$\chi_a = (A_a^T W_a A_a)^{-1} A_a^T W_a B_a \omega_a. \tag{22}$$

The actuation quantities can be extracted from χ_a in (22).

1) Steering Actuation Kinematics: For steerable wheels on many types of rovers, the axes of steering and wheel turn slip are coincident, making the steering angles ψ_i indistinguishable from turn slip ζ_i. If these steering-angle rates are included in the joint-angle rate vector $\dot{q}_a$, and thus, in the actuation vector χ_a in (21), then columns of A_a corresponding to the steering joints will be linearly dependent on the columns of A_a corresponding to the turn slips. The Jacobian matrix A_a becomes rank-deficient, and as a result, the inverse in (22) does not exist.

In this situation, we use a geometric method described below to find the steering-angle rates $\dot{\psi}_i$ based on desired forward velocity $\dot{x}_d$ and turn rate $\dot{\phi}_d$. The values of $\dot{\psi}_i$ are then used as sensed values in (20) and (21). Thus, we move the steering rates from the vector of unknown quantities $\dot{\chi}_a$ to the vector of known quantities ω_a and the corresponding columns of A_a are moved to B_a. The modified system of equations are then solved for remaining actuated variables (e.g., wheel-roll rates $\dot{\theta}_a$).

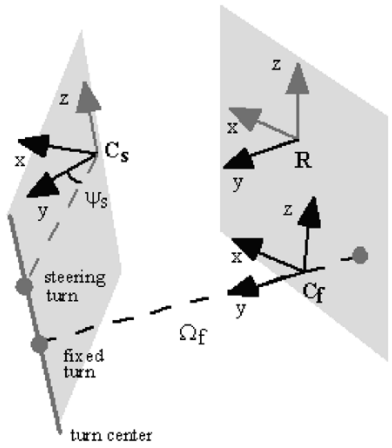

Fig. 7. Turn center corresponding to fixed wheels.

There are two steps to solving for the desired steering rates $\dot{\psi}_i$. First, we determine an instantaneous turn-center location, based on desired rover velocity and turn rates, and any nonholonomic constraints due to nonsteerable wheels. Next, we calculate steering angles corresponding to the turn-center location. Fig. 7 shows coordinate frames corresponding to a steerable wheel (C_s), a fixed wheel (C_f), and the rover reference frame (R). We index steerable wheels by $i \in N_s = \{1, 2, \ldots, n_s\}$, and fixed wheels by $i \in N_f = \{n_s + 1, \ldots, n\}$, where n_s and $n_f = n - n_s$ are the number of steerable and fixed wheels, respectively. The fixed wheels have only turn-slip rate $\dot{\zeta}_i, i \in N_f$, whereas the steerable wheels have both steering rate $\dot{\psi}_i$ and turn-slip rate $\dot{\zeta}_i, i \in N_s$.

When the rover has no fixed wheels (i.e., all wheels are steerable), the desired turn center is located along the rover's y reference axis, and the rover turn radius Ω_R is obtained from desired forward velocity $\dot{x}_d$ and turn rate $\dot{\phi}_d$ as

$$\Omega_R = \frac{\dot{x}_d}{\dot{\phi}_d}. \tag{23}$$

The turn center lies on either the left or right side of the rover, depending on the sign of the desired velocity and turn rate.

When the rover has one or more fixed wheels, the turn center must lie along the y axis of the fixed wheel in order to accomplish the turn without side slip. The turn radius for each fixed wheel is given by

$$\Omega_i = \Omega_R - D_i, \quad i \in N_f$$

where D_i is the distance from the fixed wheel-coordinate frame to the x–z plane of the rover coordinate frame, measured along the y axis of the fixed wheel. Fig. 7 illustrates the desired turn-center location for a fixed wheel by the distance Ω_f from the fixed wheel-coordinate frame C_f.

The rover reference to fixed wheel-contact transformation matrix $T_{R,Ci}$ given in Section II is used to express the desired turn-center location L_{Ri} of a fixed wheel in the rover reference frame as

$$L_{Ri} = T_{R,Ci}[0 \quad \Omega_i \quad 0 \quad 1]^T, \quad i \in N_f. \tag{24}$$

An articulated rover with multiple fixed wheels may have distinct desired turn centers given by (24), particularly on nonuniform terrain. In this case, consistent motion is not achievable, and there will be side slip of wheels. We estimate the composite turn-center location L_R, as the average of the turn-center locations of individual fixed wheels

$$L_R = \begin{cases} \dfrac{1}{n_f} \displaystyle\sum_{i \in N_F} L_{Ri}, & n_f > 0 \\ [0 \quad \Omega_R \quad 0 \quad 1]^T, & n_f = 0. \end{cases} \tag{25}$$

Next, we calculate the desired steering angle $\psi_i, i \in N_s$ for each steerable wheel using this turn-center position vector. The rover reference to steerable-wheel transformation matrix $T_{Ci,R} = (T_{R,Ci})^{-1}$ is used to obtain the turn-center position vector in the steerable-wheel coordinate frame, i.e.,

$$L_{Ri} = T_{R,Ci} L_R, \quad i \in N_s. \tag{26}$$

The steering angle is calculated from the ratio of x and y components of the steerable-wheels position vector $L_{Ri} = [x_i \ y_i \ z_i \ 1]^T$ as

$$\psi_i = \tan^{-1}\left(\frac{x_i}{y_i}\right), \quad i \in N_s. \tag{27}$$

Fig. 7 illustrates the calculation of a steering angle based on a turn-center axis. A turn-center axis is defined for each steerable wheel by the desired turn-center location and the z axis of the steerable-wheels coordinate frame C_s. The z axis, desired turn center, and resulting steering turn center all lie in the same plane.

Note that the above method of calculating steering angles is dependent only on the rover geometry and the desired rover motion. Thus, the method permits execution of the desired steering angles prior to moving the rover, which is analogous to turning the steering wheel of an automobile prior to pushing the accelerator pedal.

D. Example—Rocky 7 Kinematics Forms

The quantities in the navigation kinematics (14) for the Rocky 7 are identified by noting that pitch and roll rates are measurable, and thus $\dot{u}_s = [\dot{\phi}_x \ \dot{\phi}_y]^T, \nu_s = 2$, but the coordinates x, y, z and yaw ϕ_z are not-sensed quantities, giving $\dot{u}_n = [\dot{x} \ \dot{y} \ \dot{z} \ \dot{\phi}_z]^T, \nu_n = 4$. In addition, the rocker and bogie joint angles ρ, β_1, β_2, steering angles ψ_1, ψ_2, and wheel-roll angles θ are measurable, thus giving $\dot{p}_s = [\dot{\rho} \ \dot{\beta}_1 \ \dot{\beta}_2 \ \dot{\psi}_1 \ \dot{\psi}_2 \ \dot{\theta}]^T, \mu_s = 11$. Due to the middle and back wheel arrangements in the Rocky 7, the side-slip change $\dot{\eta}$ will be reflected as a change in $\dot{y}$. Because of the dependency of $\dot{y}$ and $\dot{\eta}$, only one of them, i.e., $\dot{y}$, can be treated as unknown and placed on the LHS of (15), and the other, i.e., $\dot{\eta}$, is removed from the equations. Similarly, due to the dependency of the roll rate $\dot{\theta}$ and roll slip rate $\dot{\xi}$, only the former is kept on the LHS of (15), and the latter is removed from the equation. Finally, since the steering is computed using a geometric approach independent of the turn-slip rate $\dot{\zeta}$, we keep the latter as an unknown quantity on the LHS of (15). Thus, the not-sensed vector $\dot{p}_n$ in (14) and (15) consists of $\dot{\zeta}$ and contact-angle rates, and thus, $\dot{p}_n = [\dot{\zeta} \ \dot{\delta}]^T$ and $\mu_n = 12$. The matrices J_n and J_s in (14) and (15) are obtained by appropriate partitioning of the

Jacobian matrices in (12) and (13). In the compact form (15), the matrices A and B have sizes $6n \times (\nu_n + \mu_n) = 36 \times 16$ and $6n \times (\mu_s + \nu_s) = 36 \times 13$, respectively. Based on analysis that was confirmed by simulations, the matrix A was found to be of full rank for normal operating ranges of Rocky 7.

The Rocky 7 quantities for slip kinematics (18) are $\dot{u}_s = [\dot{x}\ \dot{y}\ \dot{z}\ \dot{\phi}_x\ \dot{\phi}_y\ \dot{\phi}_z]^T$ and $\dot{q}_s = [\dot{\rho}\ \dot{\beta}_1\ \dot{\beta}_2\ \dot{\psi}_1\ \dot{\psi}_2]^T$. Note that all rates for position, attitude, and joint angles are sensed, and thus, $\dot{u}_n$ and $\dot{q}_n$ are removed from the LHS of (18). The submatrices J_{in} and J_{is} in (18) are obtained from appropriate partitioning of the wheel Jacobian matrices in (12) and (13). In the compact form (19), the matrices A_i are $6 \times (\mu_n + \nu_{qn} + 4) = 6 \times 4$ for all wheels, while the matrices B_i are $6 \times (\mu_s + \nu_{qs} + 1) = 6 \times (6 + 2 + 1) = 6 \times 9$ for all wheels. Based on analysis of the Jacobian matrices in (12) and (13) and simulations, the matrices A_i have full rank for normal operating ranges of Rocky 7.

Now consider the actuation kinematics. Wheels 1 and 2 of Rocky 7 have steering axes coincident with the wheel-slip axes, such that (20) is underdetermined. We therefore apply the analysis of Section III-C.1 to determine steering actuation values ψ_1 and ψ_2. The steerable wheel set for Rocky 7 is $N_s = \{1, 2\}$, and the fixed wheel set is $N_f = \{3, 4, 5, 6\}$. Each of the four fixed wheels produces a candidate turn-center position L_{Ri} obtained by substituting (11) into (24). These are averaged according to (25) to yield (28), shown at the bottom of the page. Note that the y component of (28) is obtained from (23), and depends only on the desired rover kinematics (i.e., forward velocity and turn rate), while the x and z components depend only on the rover geometrical configuration (e.g., joint angles and link distances).

The next step is to calculate the steering actuation values $\psi_i, i = 1, 2$ corresponding to each of the two steerable wheels. This is achieved by determining $T_{Ci,R} = (T_{R,Ci})^{-1}$ via (10) and substituting the results together with (28) into (26) to get $L_{R_i}, i = 1, 2$. The steering angles $\psi_i, i = 1, 2$ of the front wheels are then obtained using (27).

In order to find the wheel-roll actuation quantities $\dot{\theta}$, we employ (20). It is noted that the rocker and bogie joints are unactuated, and steering actuation values are already determined using the geometric approach. Thus, $\dot{q}_a$ and $\dot{q}_{un}$ are removed from (20). Similarly, all wheel rolling angles are actuated, thus $\dot{\theta}_s$ is removed, and $\dot{\theta}_a$ and $\dot{\theta}_{un}$ are combined to form $\dot{\theta}_a$. We rearrange (20) to obtain

$$[E_n \quad -J_{an}] \begin{bmatrix} \dot{u}_n \\ \dot{\theta}_a \\ \dot{\zeta} \\ \dot{\delta} \end{bmatrix} = [-E_{ds} \quad J_{as}] \begin{bmatrix} \dot{u}_d \\ \dot{u}_s \\ \dot{q}_s \end{bmatrix} \tag{29}$$

where $\dot{u}_n = [\dot{y}\ \dot{z}]^T, \dot{u}_d = [\dot{x}_d\ \dot{\phi}_z]^T$ is the desired forward speed and heading, $\dot{u}_s = [\dot{\phi}_x\ \dot{\phi}_y]^T$ is the vector of measured pitch and roll rates, and $\dot{q}_s = [\dot{\rho}\ \dot{\beta}_1\ \dot{\beta}_2\ \dot{\psi}_1\ \dot{\psi}_2]^T$ are sensed joint angles. Thus, in the compact form (21), A_a has dimensions $6n \times (\mu_n + \nu_{an}) = 36 \times (2 + 18) = 36 \times 20$, and B_a has dimensions $6n \times (\mu_{ds} + \nu_{as}) = 36 \times (4 + 5) = 36 \times 9$. Based on simulations and analyses, the matrix A_a is full rank under normal operating conditions for Rocky 7. Thus, (29) can be solved for the wheel-roll actuation quantities $\dot{\theta}_a$ using a least-squares method similar to (17).

IV. Simulation of Rover–Terrain Interaction

The navigation, actuation, and slip kinematics equations use the sensed quantities that are available on most rovers. The Rocky 7 rover, for example, provides sensing of rocker and bogie joint angles, wheel-rolling rates, and rover body pitch and roll. This information is readily available whenever the rover traverses actual terrain. However, it is expensive and time-consuming to perform experiments with rovers on actual terrain for investigation purposes. Therefore, we developed a simulation of rover motion over a given terrain. Such a terrain is supplied either using images of an actual terrain and extracting elevation Z_{ter} at different (X, Y) positions, or employing any function $Z_{\text{ter}}(X, Y)$ which returns elevation of the terrain. We are concerned here only with the topology of the terrain, not surface conditions (e.g., sandy, rough, slippery). The objective is to estimate the sensed quantities when the rover moves over a given terrain topology, and use these sensed quantities for verifying the navigation, slip, and actuation kinematics.

Consider the rover configuration vector in the world-coordinate frame $U = [X\ Y\ Z\ \Phi_x\ \Phi_y\ \Phi_z]^T$. The transformation matrix relating the wheel-terrain contact frames $C_i, i = 1, \ldots, n$ to the world-coordinate frame W is

$$T_{W,Ci}(U, q, \delta_i) = T_{W,R}(U) T_{R,Ai}(q) T_{Ai,Ci}(\delta_i) \tag{30}$$

where $T_{R,Ai}(q)$ is the transformation matrix from rover reference to wheel-axle frames, which is dependent on the joint-angle vector q of the linkage mechanism connecting the rover to the wheel axles, and $T_{Ai,Ci}(\delta_i)$ is the axle-to-contact-frames transformation given by (1). Since $T_{W,Ci}$ is a standard homogeneous transformation matrix, it is used to extract the position and orientation of the wheels at the terrain contact as

$$\begin{bmatrix} X_i(U, q, \delta_i) \\ Y_i(U, q, \delta_i) \\ Z_i(U, q, \delta_i) \\ \Phi_{xi}(U, q, \delta_i) \\ \Phi_{yi}(U, q, \delta_i) \\ \Phi_{zi}(U, q, \delta_i) \end{bmatrix} = \begin{bmatrix} T_{W,Ci}[1,4] \\ T_{W,Ci}[2,4] \\ T_{W,Ci}[3,4] \\ a\tan(T_{W,Ci}[3,2]/T_{W,Ci}[3,3]) \\ a\sin(-T_{W,Ci}[3,1]) \\ a\tan(T_{W,Ci}[2,1]/T_{W,Ci}[1,1]) \end{bmatrix} \tag{31}$$

where $i = 1, 2, \ldots, n$, $T_{W,Ci}[j,k]$ denotes the element on the intersection of the jth row and kth column of the transformation matrix, and it is assumed that the pitch is limited to $-\pi/2 < \Phi_{yi} < \pi/2$.

$$L_R = \begin{bmatrix} \frac{1}{4}\sum_{i=3}^{6} k_6 c(k_9 - b_i\rho) + a_{Si} c(\sigma_i - \delta_i) - k_8 s(\sigma_i - \delta_i) - k_{10} s(\sigma_i) \\ \Omega_R \\ \frac{1}{4}\sum_{i=3}^{6} -k_6 s(k_9 - b_i\rho) - a_{Si} s(\sigma_i - \delta_i) - k_8 c(\sigma_i - \delta_i) - k_{10} c(\sigma_i) \end{bmatrix} \tag{28}$$

Suppose that the terrain elevation is given by $Z_{\text{ter}}(X, Y)$. If the rover has a wheel in contact with the terrain, then the elevation of the terrain at the wheel-contact location given by (31) must be equal to the Z component of the contact location, i.e., the contact error

$$E_i(U, q, \delta_i) = Z_i(U, q, \delta_i) - Z_{\text{ter}}(X_i, Y_i) \tag{32}$$

must be zero. When $E_i(U, q, \delta_i) = 0$, wheel i just touches the terrain, whereas $E_i(U, q, \delta_i) > 0$ implies that the wheel is above the terrain, and $E_i(U, q, \delta_i) < 0$ indicates the wheel penetrates the terrain.

For our purposes of simulating rover–terrain interaction, we determine the values of U, q, and δ that minimize the contact errors, so as to best fit the wheels to the terrain. The free variables in this optimization problem are (Z, Φ_x, Φ_y, q). The rover position (X, Y) and heading Φ_z are fixed by the desired rover path. The contact angle for each wheel δ_i is determined as $\delta_i = a\tan(\lambda_i)$, where λ_i is the terrain slope at the wheel position (X_i, Y_i) along the wheel heading Φ_{zi}. This method assumes that each wheel has a single point of contact with a smooth terrain (i.e., continuous-terrain slope). We also assume nondeformable terrain and that all wheels are in contact with the terrain. These assumptions were made to simplify the optimization requirements.

We now define $E(Z, \Phi_x, \Phi_y, q)^T$ as the $n \times 1$ vector whose ith component is $E_i(Z, \Phi_x, \Phi_y, q)$. The norm of the error vector provides an objective function $\eta(Z, \Phi_x, \Phi_y, q)$ for minimizing all wheel-contact errors, i.e.,

$$\eta(Z, \Phi_x, \Phi_y, q) = E^T(Z, \Phi_x, \Phi_y, q)\, E(Z, \Phi_x, \Phi_y, q). \tag{33}$$

At each time step Δt, we solve the nonlinear optimization problem (33) to find the free parameters, namely, rover elevation Z, pitch Φ_y, roll Φ_x, and joint-angle vector q. We use the "fminbnd" optimization function provided by Matlab. This line-search method uses Golden Section search and parabolic interpolation. We iteratively apply the line-search function to each free variable until we converge on a solution. The result is a rover configuration that conforms to the terrain for the given position (X, Y) and heading Φ_z. Wheel-rolling rates $\dot{\theta}_i$ are obtained from estimates of how much each wheel rolled between two consecutive time steps.

In summary, the wheel-terrain contact, terrain optimization, and wheel-rolling rates described above represent a simulated rover model. The inputs to this model are the terrain geometry $Z_{\text{ter}} = (X, Y)$, the current rover position (X, Y), and heading Φ_z. The output of the rover model are the sensed quantities, such as rover pitch Φ_x, roll Φ_y, joint-angle vector q, elevation Z, contact angles δ_i, and wheel-rolling angle θ_i. We also developed an animation package using Matlab/Simulink. Fig. 8 shows a snapshot of the animation as the rover moves over an uneven terrain. It embodies the kinematics and rover–terrain interaction model and continuously displays rover quantities such as position, orientation, and joint angles. It also allows zooming in and out and observing various views, e.g., top, down, and side.

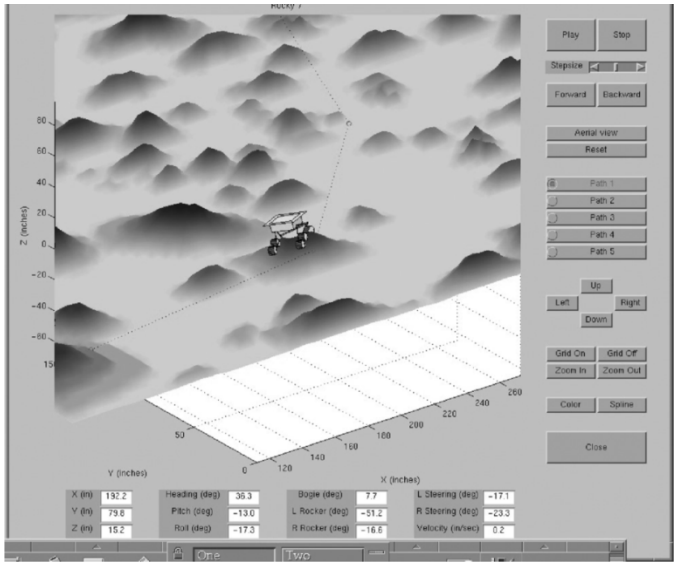

Fig. 8. Snapshot of the rover animation.

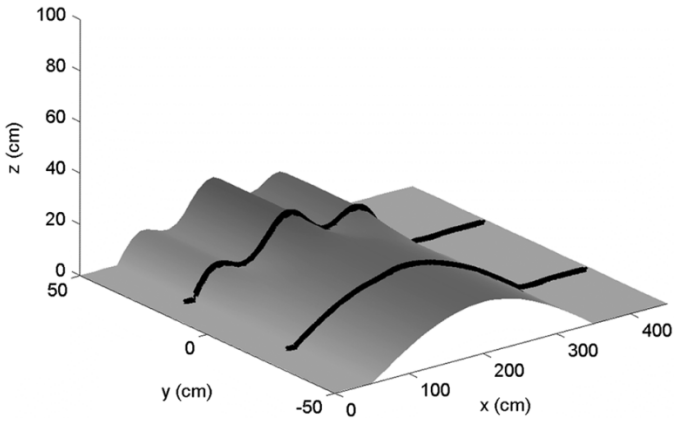

Fig. 9. Traces of front wheels over unsymmetrical wavy bump.

V. Simulation Results

In this section, we investigate actuation and slip kinematics for the Rocky 7 rover with the purpose of studying the behavior of the rover as it moves over simulated terrains. The terrain–rover interaction model described in Section IV will represent the simulated rover. We consider two cases of terrain topology and rover path, as given in Sections V-A and V-B below. In Section V-C, we provide simulation results for kinematics sensitivity to noise.

A. Unsymmetrical Wavy-Bump Terrain—Straight Path

The terrain, as shown in Fig. 9, consists of a bump which is wavy (sinusoidal) on the left and smooth on the right. The left side of the rover, consisting of wheels 1, 3, and 5, move over the wavy side, while its right side wheels 2, 4, and 6 traverse the smooth side of the bump. The rover moves on a straight path with a constant speed of 1 cm/s. The traces of the front wheels are shown in Fig. 9. The rover reference point is at the origin $(X = Y = 0)$ at time $t = 0$.

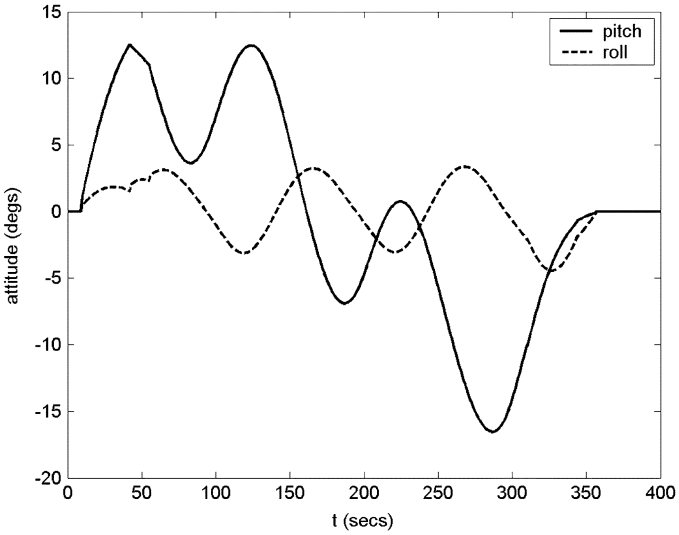

Fig. 10. Rover roll and pitch for straight path.

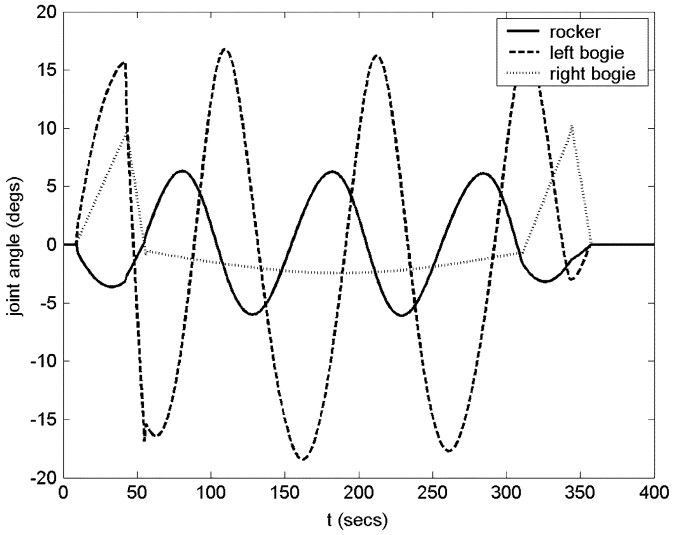

Fig. 11. Rocker and bogie joint angles for straight path.

Fig. 10 shows the rover body roll Φ_x and pitch Φ_y as the results of combined motion of six wheels. When the rover reference point moves about 9.1 cm, the front wheels hit the bump at $X = 50$ cm (Fig. 9), the rover pitch changes from zero to a positive value, and then oscillates due to the wavy-terrain profile. The rover pitch is initially positive until the rover reaches the top of the bump. The rover roll oscillates due to a different terrain profile under the right and left wheels. Note the roll trajectory during the transition from where all wheels are on the flat surface to where the front wheels hit the bump, and finally to where all wheels are on the bump, at which point the rover roll reflects the wavy surface.

Fig. 11 shows the rover joint angles, including the rocker angle ρ and left and right bogie angles β_1 and β_2. The rocker and left bogie angles, ρ and β_1, oscillate as the left wheels traverse the wavy bump. There are both amplitude and phase differences between ρ and β_1, with the rocker having a lower amplitude than the left bogie, due to the fact that the bogie is shorter in length

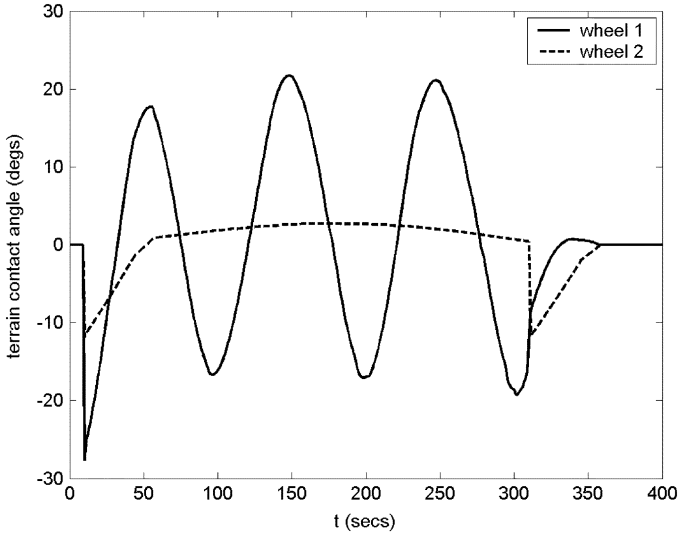

Fig. 12. Contact angle for the front wheels on a straight path.

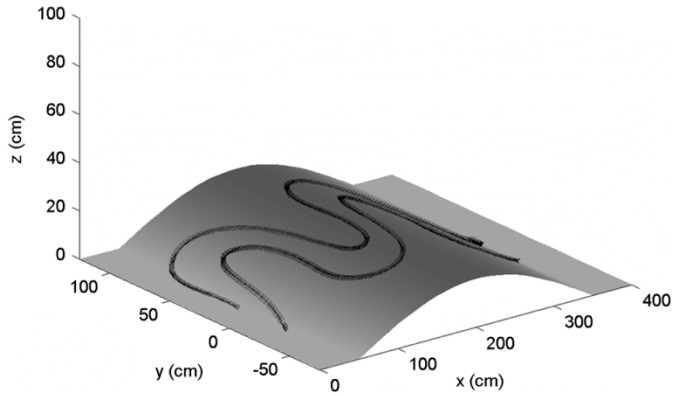

Fig. 13. Traces of front wheels for a serpentine path.

than the rocker (see Fig. 5). The right bogie experiences transitions between the time when the middle and back wheels hit the bump, and again when these two wheels leave the bump. Note that the right bogie does not oscillate, since the terrain is smooth on the right side.

Fig. 12 shows the contact-angle trajectories for the front wheels. Although not shown, the rear-wheel contact angles behave similarly. The contact angles experience a sudden change as the wheels hit the bump, and then the contact angles on the left side oscillate due to the wavy terrain.

The wheels also exhibit side slip as a result of the unsymmetrical terrain profile under the left and right sides of the rover. However, the amount of side slip is small, since there is no steering or turns.

B. Bumpy Terrain—Serpentine Path

The purpose of simulations in this section is to study the behavior of the rover while turning. The terrain shown in Fig. 13 is similar to the previous case, but the bump has no waves. Including the waves would mix various behaviors in a complex manner, and make it very hard to observe the turning characteristics of the rover. The rover has the same speed of 1 cm/s as

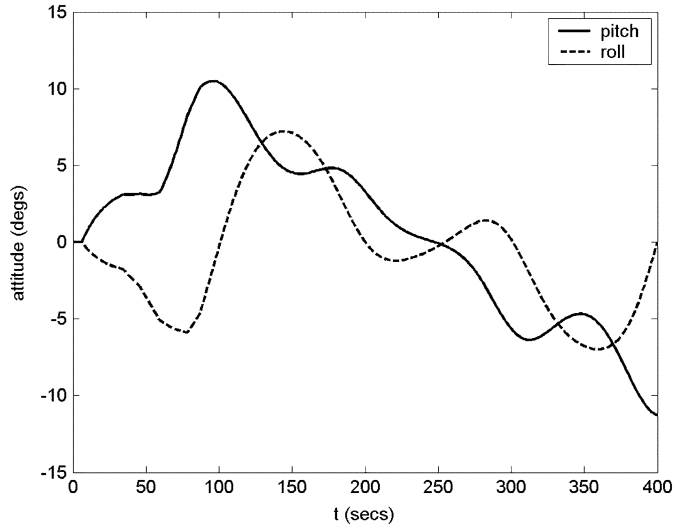

Fig. 14. Rover pitch and roll for a serpentine path.

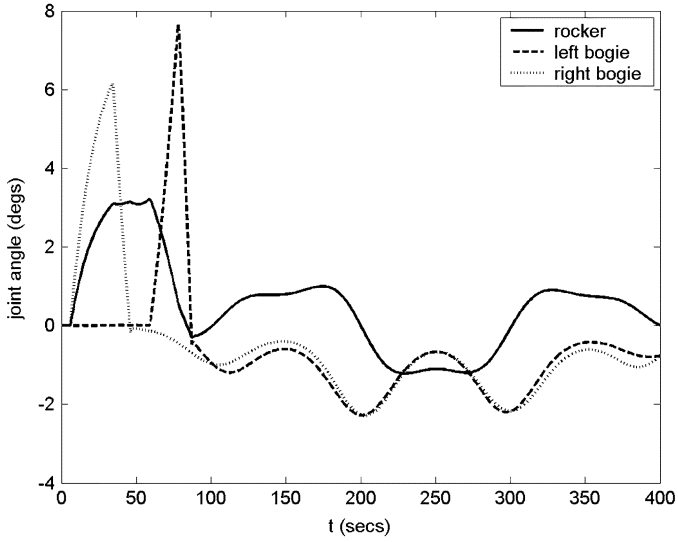

Fig. 15. Rocker and bogie joint angles for a serpentine path.

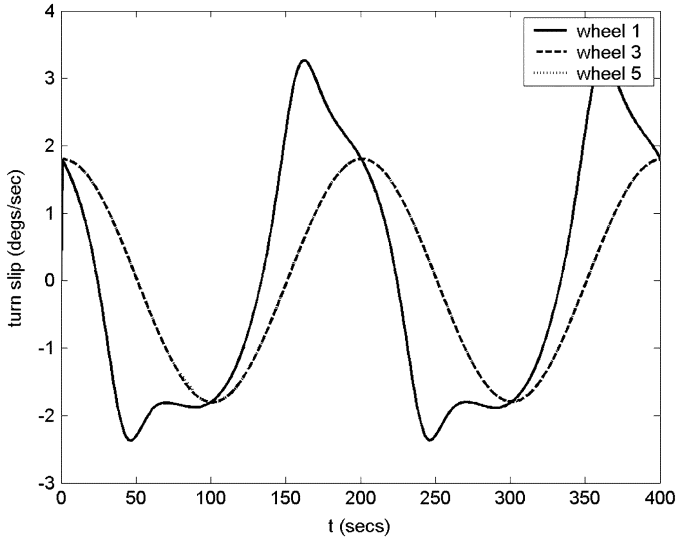

Fig. 16. Wheel turn slips for left wheels.

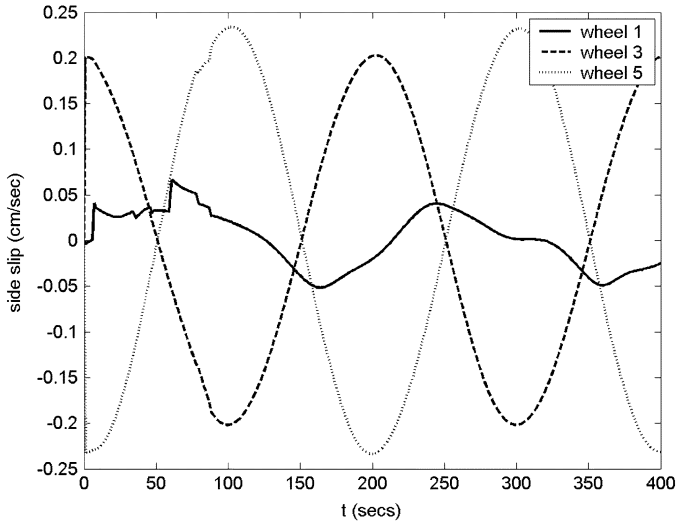

Fig. 17. Wheel side slips for left wheels.

before, but now moves in a serpentine path with a yaw angle given by $\Phi_y = \sin(\pi t/100)$.

The rover pitch Φ_x and roll Φ_y are shown in Fig. 14. The pitch starts out positive until the rover is on top of the bump, and becomes negative as the rover moves down the hill. The serpentine trajectory causes the pitch to oscillate as the rover alternately turns left and then right across the hill. The roll starts out negative due to the serpentine path, and then oscillates for same reason as pitch. The complex behavior of the pitch and roll is also influenced by the rocker-bogie design of Rocky 7. The effect is most apparent during the first 80 s, as the individual wheels encounter the start of the bump. The rocker and bogie angles ρ, β_1, and β_2 are depicted in Fig. 15. All three quantities exhibit a sudden change as the rover hits the bump, but the serpentine path is such that the right front wheel reaches the bump before the left wheel, so the right bogie angle leads that of the left.

The actuated steering angles ψ_1 and ψ_2 are not shown, but have sinusoidal trajectories. The wheel inside the turn has a smaller steering angle than the wheel on the outside of the turn.

Because of the particular terrain and path, all three types of slips occur. The turn-slip rates for the left wheels 1, 3, and 5 are shown in Fig. 16. The turn slip for steerable wheel 1 is less sinusoidal than wheels 3 and 5. The latter two exhibit almost identical turn-slip rates, and are indistinguishable in Fig. 16. The middle and rear wheels are nonsteerable, and thus have significantly more rolling and side slip during turns than the front steerable wheels. The side-slip rates are illustrated in Fig. 17. The middle and back wheels have opposite side-slip rates, such that one slips toward inside while the other slips toward outside of the turn. The nonsmooth behaviors for all slips during the first 80 s are due to the rocker-bogie effects, as mentioned before. Results for the right wheels 2, 4, and 6 are not shown, but have similar behaviors.

C. Sensitivity to Sensor Noise

The proposed kinematics models use sensed quantities to determine unknown rates such as slip. However, sensor errors and

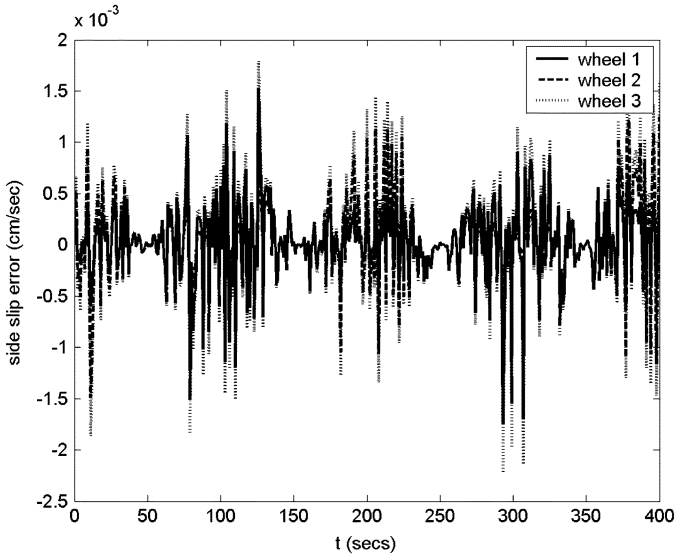

Fig. 18. Side-slip estimation error to noise in $\dot{y}$.

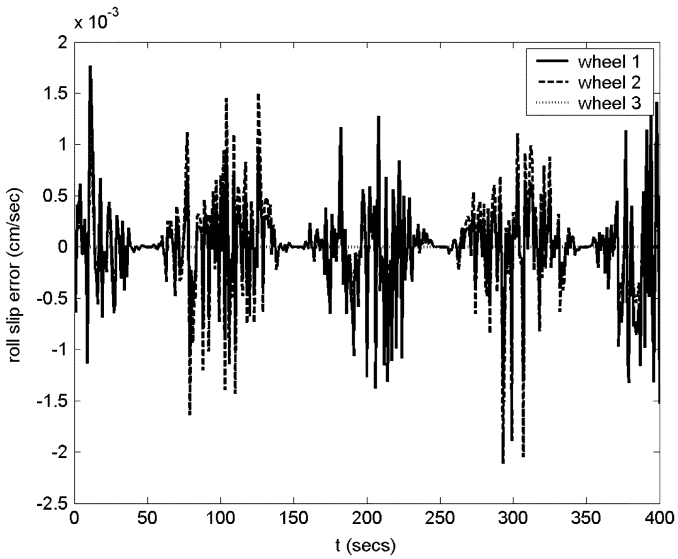

Fig. 19. Roll-slip estimation error to noise in $\dot{y}$.

noise can degrade the ability to accurately detect desired quantities. We investigated the effects of sensor noise on slip kinematics using a normal distribution on selected sensed quantities, including wheel-rolling rates $\dot{\theta}$ and rover body rates $\dot{x}$ and $\dot{y}$. Fig. 18 shows the error in detected side slip for wheels 1, 2, and 3 given a 5% standard deviation noise in $\dot{y}$ while following the serpentine path shown in Fig. 13. Since the sensed $\dot{y}$ is noisy, the side slip is also noisy, and we see a pattern where the errors are largest when $\dot{y}$ is highest (i.e., during sharp turns). It is noted from Fig. 18 that the noise affects middle wheel 3 (and also other back wheels) more than the steerable front wheels 1 and 2. Furthermore, comparing Figs. 18 and 17, we observe that the error due to the sensor noise is two orders of magnitude smaller than the detected side slip. Thus, the sensor noise would have to be much larger to significantly degrade side-slip detection. A similar result is obtained for roll slip. As shown in Fig. 19, the effect of $\dot{y}$ sensor noise on roll slip is very small. It is also noted that unlike the side slip, noise affects the roll slip of front wheels more than back wheels, as expected. Similar behaviors were seen for noise in the body rate $\dot{x}$ and wheel-rolling rates $\dot{\theta}$, although noise on these sensors has a more pronounced effect on the detected slip. These results suggest that there are situations where slip information can still be extracted under the effects of small or moderate sensor noise.

It should be noted that detected slip rates are linearly dependent on the sensed quantities, as seen in (18), so that noise affects slip detection proportionally. However, the proportionality coefficient depends on the particular rover configuration including joint angles and terrain contacts. A rigorous mathematical sensitivity analysis can be performed, but is beyond the scope of this paper.

VI. Conclusion

A methodology has been presented for developing kinematic models of articulated rovers. The kinematic model allows full 6-degree-of-freedom motion, and is applicable to any high-mobility wheeled rover traversing uneven terrain. Three types of kinematics are identified in the paper, including navigation, slip, and actuation. In particular, slip kinematics can be used to detect various wheels slips for proper wheel actuation in order to reduce undesirable motions.

Actuation kinematics makes it possible to determine individual wheel speed and steering commands to achieve coordinated motion. This is important, since a rover moving on a bumpy surface may require its individual wheels to travel different distances to maintain the desired motion.

Another feature of the paper is the development of a method to determine wheel-steering angles for rovers where the axis of steering and wheel turn slip are coincident. This common rover design makes it impossible to determine the steering command using kinematics, since the wheel Jacobian matrices become rank-deficient. A combined geometric-kinematic approach is proposed to resolve the problem.

The kinematic modeling and analysis has been applied to a prototype Mars rover which has a relatively complex mobility system. Simulation studies show the motion of the rover over several terrain topologies. The acquired trajectories of rover joint angles, rover orientation angles, and wheel actuation command are consistent and agree with the expected results.

Finally, there are several limitations of the proposed kinematic models and analyses that we are currently investigating. The proposed terrain-interaction model assumes a single point of contact between the wheel and a continuous, smooth terrain. For rugged terrain, there may be multiple contact points and sudden, discontinuous changes in the point of contacts (e.g., traversal over rocks), for which the rates (derivatives) are infinite. Furthermore, the terrain may be deformable (e.g., sand), such that the wheel and terrain interactions become substantially more complicated. Also, some wheels may not always be in contact with the terrain. There are also dynamics effects that can influence the rover–terrain interaction. Nevertheless, the proposed models and analyses should provide useful tools for studying behaviors of articulated rovers under a variety of situations and terrain topologies. They can also be used at the design stage to

investigate the rover performance under different kinematics arrangements and parameters.

APPENDIX

Elements of the second through sixth rows of the Jacobian matrix for front wheels ($i = 1, 2$) of Rocky 7 are given here. The contributions of various joint angles to side motion are relatively simple and given by

$$\begin{aligned}
J_{y,\psi} &= k_4 + k_2 c\rho + b_i k_1 s\rho \\
J_{y,\theta} &= k_{10} s\psi_i c\delta_i \\
J_{y,\xi} &= s\psi_i c\delta_i \\
J_{y,\zeta} &= -k_5 c\psi_i s\delta_i - k_4 c\delta_i - k_1(b_i s\rho c\delta_i - c\rho c\psi_i s\delta_i) \\
&\quad - k_2(c\rho c\delta_i + b_i s\rho c\psi_i s\delta_i) \\
J_{y,\eta} &= c\psi_i \\
J_{y,\delta} &= -k_5 s\psi_i + k_1 c\rho s\psi_i - b_i k_2 s\rho s\psi_i.
\end{aligned}$$

The third row defines contributions of various angles to the vertical motion of the rover as follows:

$$\begin{aligned}
J_{z,\psi} &= k_3 s\rho \\
J_{z,\theta} &= k_1(b_i s\rho c\psi_i c\delta_i - c\rho s\delta_i) \\
J_{z,\xi} &= b_i s\rho c\psi_i c\delta_i - c\rho s\delta_i \\
J_{z,\zeta} &= b_i k_5 s\rho s\psi_i s\delta_i + k_4 c\rho s\psi_i s\delta_i + b_i k_3 c\rho c\psi_i s\delta_i \\
&\quad - k_3 s\rho c\delta_i + k_2 s\psi_i s\delta_i \\
J_{z,\eta} &= -b_i s\psi_i s\rho \\
J_{z,\delta} &= -b_i k_5 s\rho c\psi_i - k_4 c\rho c\psi_i + b_i k_3 c\rho s\psi_i - k_2 c\psi_i.
\end{aligned}$$

The last three rows determine the contributions of rover joints to the orientation of the rover, and are given by

$$\begin{aligned}
J_{\phi x,\psi} &= b_i s\rho, \\
J_{\phi x,\zeta} &= c\rho c\psi_i s\delta_i - b_i s\rho c\delta_i \\
J_{\phi x,\delta} &= c\rho s\psi_i \\
J_{\phi y,\zeta} &= s\psi_i s\delta_i \\
J_{\phi y,\delta} &= -c\psi_i \\
J_{\phi z,\psi} &= -c\rho \\
J_{\phi z,\zeta} &= c\rho c\delta_i + b_i s\rho c\psi_i s\delta_i \\
J_{\phi z,\delta} &= b_i s\rho s\psi_i.
\end{aligned}$$

The elements of the Jacobian matrix (13) for the middle and back wheels ($i = 3, 4, 5, 6$) are as follows:

$$\begin{aligned}
J_{x,\beta 1} &= \frac{1}{2}(b_i - 1)(k_6 s(k_9 + \rho) - k_1) \\
J_{x,\beta 2} &= -\frac{1}{2}(b_i + 1)(k_6 s(k_9 - \rho) - k_1) \\
J_{x,\zeta} &= -b_i k_3 c\sigma_i \\
J_{x,\delta} &= -k_6 s(k_9 - b_i\rho) - a_{si} s(\sigma_i - \delta_i) \\
&\quad - k_8 c(\sigma_i - \delta_i) + k_1 \\
J_{y,\zeta} &= -k_6 c(k_9 - b_i\rho - \sigma_i) - a_{si} c\delta_i \\
&\quad - k_8 s\delta_i + k_1 s\sigma_i - k_2 c\sigma_i \\
J_{z,\beta 1} &= \frac{1}{2}(b_i - 1)(k_6 c(k_9 + \rho) + k_2) \\
J_{z,\beta 2} &= -\frac{1}{2}(b_i + 1)(k_6 c(k_9 - \rho) + k_2) \\
J_{z,\zeta} &= b_i k_3 s\sigma_i \\
J_{z,\delta} &= -k_6 c(k_9 - b_i\rho) - a_{si} c(\sigma_i - \delta_i) \\
&\quad + k_8 s(\sigma_i - \delta_i) - k_2 \\
J_{\phi y,\beta 1} &= \frac{1}{2}(b_i - 1) \\
J_{\phi y,\beta 2} &= -\frac{1}{2}(b_i + 1)
\end{aligned}$$

where a_{si} and σ_i are defined after (11).

ACKNOWLEDGMENT

The authors gratefully acknowledge the support of Dr. S. Hayati of JPL, and thanks are also due to Dr. R. Volpe and Dr. B. Balaram of JPL.

REFERENCES

[1] S. Hayati *et al.*, "The Rocky 7 rover: A Mars sciencecraft prototype," in *Proc. IEEE Int. Conf. Robot. Autom.*, Albuquerque, NM, 1997, pp. 2458–2464.

[2] Ch. DeBolt, Ch. O'Donnell, S. Freed, and T. Nguyen, "The bugs "basic uxo gathering system" project for uxo clearance and mine countermeasures," in *Proc. IEEE Int. Conf. Robot. Autom.*, Albuquerque, NM, 1997, pp. 329–334.

[3] A.-J. Baerveldt, Ed., *Agricultural Robotics, Autonomous Robots*. Norwell, MA: Kluwer, 2002, vol. 13-1.

[4] P. S. Schenker, P. Pirjanian, B. Balaram, K. S. Ali, A. Trebi-Ollennu, T. L. Huntsberger, H. Aghazarian, B. A. Kennedy, E. T. Baumgartner, K. Iagnemma, A. Rzepniewski, S. Dubowsky, P. C. Leger, D. Apostolopoulos, and G. T. McKee, "Reconfigurable robots for all terrain exploration," *Proc. SPIE*, vol. 4196 , pp. 15–22, Nov. 2000.

[5] I. J. Cox and G. T. Wilfong, *Autonomous Robot Vehicles*. New York: Springer-Verlag, 1990.

[6] K. Iagnemma, F. Genot, and S. Dubowski, "Rapid physics-based rough terrain rover planning with sensor and control uncertainty," in *Proc. IEEE Int. Robot. Autom.*, Detroit, MI, 1999, pp. 2286–2291.

[7] P. F. Muir and C. P. Neumann, "Kinematic modeling of wheeled mobile robots," *J. Robot. Syst.*, vol. 4, no. 2, pp. 282–340, 1987.

[8] J. C. Alexander and J. H. Maddocks, "On the kinematics of wheeled mobile robots," *Int. J. Robot. Res.*, vol. 8, no. 5, pp. 15–26, 1989.

[9] G. Campion, G. Bastin, and B. Dandrea-Novel, "Structural properties and classification of kinematic and dynamic models for wheel mobile robots," *IEEE Trans. Robot. Autom.*, vol. 12, no. 1, pp. 47–62, Feb. 1996.

[10] J. Borenstein, "Control and kinematics design of multi-degree of freedom robots with compliant linkage," *IEEE Trans. Robot. Autom.*, vol. 11, no. 1, pp. 21–35, Feb. 1995.

[11] R. Rajagopalan, "A generic kinematic formulation for wheeled mobile robots," *J. Robot. Syst.*, vol. 14, no. 2, pp. 77–91, 1997.

[12] B.-J. Yi and W. K. Kim, "The kinematics for redundancy actuated omnidirectional mobile robots," *J. Robot. Syst.*, vol. 19, no. 6, pp. 255–267, 2002.

[13] R. L. Williams, B. E. Carter, P. Gallina, and G. Rosati, "Dynamic model with slip for wheeled omnidirectional robots," *IEEE Trans. Robot. Autom.*, vol. 18, no. 3, pp. 285–293, Jun. 2002.

[14] M. Tarokh, G. McDermott, S. Hayati, and J. Hung, "Kinematic modeling of a high-mobility Mars rover," in *Proc. IEEE Int. Conf. Robot. Autom.*, Detroit, MI, 1999, pp. 992–998.

[15] K. Iagnemma and S. Dubowski, "Vehicle-ground contact angle estimation with application to mobile robot traction," in *Proc. 7th Int. Conf. Adv. Robot Kinematics*, 2000, pp. 137–146.

[16] J. Balaram, "Kinematic observers for articulated rovers," in *Proc. IEEE Int. Conf. Robot. Autom.*, San Francisco, CA, 2000, pp. 2597–2604.

[17] R. Volpe, "Navigation results from desert field tests of the Rocky 7 Mars rover prototype," *Int. J. Robot. Res.*, vol. 18, no. 7, pp. 669–683, Jul. 1999.

[18] J. J. Craig, *Introduction to Robotics*, 2nd ed. Reading, MA: Addison-Wesley, 1989.

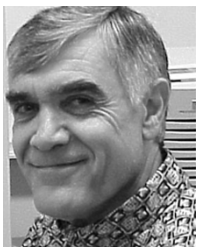

Mahmoud Tarokh received the B.S. degree from Tehran Polytechnic University, Tehran, Iran, the M.S. degree from the University of Birmingham, Birmingham, U.K., and the Ph.D. degree from the University of New Mexico, Albuquerque, all in electrical and computer engineering.

He has held academic positions at Sharif University of Technology, Tehran, Iran (1977–1985), University of Colorado, Boulder (1978–1979), University of California at San Diego, La Jolla (1987–1990), and San Diego State University, San Diego, CA (1990–present). He is currently a Professor of Computer Science and Director of the Intelligent Machines and Systems Laboratory, San Diego State University. He has published extensively in the area of robot control and path planning. His recent research work has been in the field of rover kinematics, navigation, and control.

Gregory J. McDermott received the B.S. degree in aerospace engineering from the University of Colorado, Boulder in 1982, and the M.S. degree in applied mathematics from San Diego State University (SDSU), San Diego, CA, in 1994.

He joined General Dynamics' Convair Division in 1983, working in the areas of mission planning and analysis for cruise missiles. He has extensive experience in the areas of vehicle performance modeling, automated routing, optimization, and C4ISR. He is currently with BAE Systems, San Diego, CA, doing research and development in the areas of automated mission planning and battle management. As a part-time Research Associate with SDSU, he has been supporting research projects in the areas of rover kinematics and control. His research interests include combinatorial optimization and cooperative planning in dynamic environments.